

Dispersive FDTD Scheme and Surface Impedance Boundary Condition for Modeling Pulse Propagation in Very Lossy Medium

Zhi-Hong Lai and Jean-Fu Kiang 

Abstract—A dispersive surface impedance boundary condition (SIBC) is implemented in a dispersive finite-difference time-domain (FDTD) scheme to model pulse propagation and scattering from an aquifer, which has high permittivity and high conductivity. A quadratic complex rational function (QCRF) is adopted to model the dispersive media over a wide frequency band for implementing the dispersive FDTD scheme. The proposed method is demonstrated by simulating the operation of ground-penetrating radar (GPR) in detecting water table. Group delay and pulse-broadening parameter (PBP) are defined to analyze the deformation of pulses propagating in a dispersive lossy medium.

Index Terms—Boundary conditions, electromagnetic propagation in absorbing media, finite difference methods, ground-penetrating radar (GPR), numerical simulation, soil moisture, surface impedance.

I. INTRODUCTION

GROUND-penetrating radars (GPRs) have been widely used to evaluate the condition of bridges, roads, and railways [1], ice profile and glaciology [2], and soil and liquid contamination [3]; to detect ground water [4], landmine, and unexploded ordnance (UXO) [5]; and so on. Numerical modeling techniques on GPR forward problem have been widely developed to understand the scattering mechanism underground [5]–[7]. FDTD as one of the most popular numerical modeling techniques on GPR was proposed by Yee [8] and various FDTD techniques have been developed for different applications [9], including unconditionally stable FDTD [10], domain-decomposition FDTD [11], dispersive FDTD [12], and so on. The unconditionally stable FDTD methods were proposed to mitigate the Courant–Friedrich–Levy (CFL) limitation on time steps [10], the domain-decomposition FDTD method was proposed to solve problems with very large computational domain [11], and the dispersive FDTD methods were designed for problems involving dispersive media [12].

Manuscript received March 19, 2019; revised November 5, 2019; accepted November 19, 2019. Date of publication January 8, 2020; date of current version April 7, 2020. This work was supported in part by the Air Force Office of Scientific Research, USA, under Award FA2386-19-1-4064, and in part by the Ministry of Science and Technology, Taiwan, under Contract MOST 107-2221-E-002-077. (Corresponding author: Jean-Fu Kiang.)

Zhi-Hong Lai is with MediaTek, Hsinchu, Taiwan.

Jean-Fu Kiang is with the Graduate Institute of Communication Engineering, National Taiwan University, Taipei 106, Taiwan (e-mail: jfkiang@ntu.edu.tw).

Color versions of one or more of the figures in this article are available online at <http://ieeexplore.ieee.org>.

Digital Object Identifier 10.1109/TAP.2019.2963615

Pulses emitted from typical GPRs contain frequency components in 20–1000 MHz, hence the effective wavelength in soils, with effective dielectric constant around $\epsilon_{re} = 9$, falls in the range of 0.1–5 m. The permittivity and conductivity of soils vary with frequency, neglecting their frequency dependence may induce substantial errors in retrieving geometrical parameters from the received signals [6], [13]–[15]. In [13], a multidimensional Fourier pseudospectral time-domain (PSTD) algorithm was used to simulate GPR measurements in dispersive medium and nondispersive medium. The reflected signals from a dispersive medium display different features, compared to those from a nondispersive medium. In [15], a 3-D piecewise linear recursive convolution (PLRC) finite-difference time-domain (FDTD) algorithm was implemented to simulate a GPR system for detecting different objects immersed in different types of dispersive soil, which were modeled as two-term Debye media.

A quadratic complex rational function (QCRF) was used to characterize the properties of complicated dispersive media like human tissues [16], concrete materials [17], and thin-film solar cells [18]. Numerical accuracy of QCRF applied to an FDTD scheme was investigated in [19]. In [12], a double averaging technique was reported to achieve more accurate results than using direct FDTD implementation.

A frequency-domain surface impedance boundary condition (SIBC), which relates the tangential electric field and magnetic field on the interface between two adjacent media, was introduced by Leontovich [20] in the 1940s and developed by Senior [21] in 1960. The SIBC can be used to substitute the field distribution in a spatial volume by those on its boundary surface, significantly reducing the number of unknowns and the computational load in numerical implementation. The concept of time-domain surface impedance received little attention until 1990s. Beggs *et al.* [22] introduced an SIBC valid at a given frequency and a dispersive SIBC over a frequency band. An SIBC can be implemented as a time-domain convolution if the medium is nondispersive. In [23], a method was proposed to implement a dispersive SIBC as a time-domain convolution in modeling a dispersive coating.

In this article, a time-domain SIBC is implemented in the middle of a dispersive medium, in conjunction with a dispersive FDTD scheme in the medium on one side of the SIBC. Group delay and pulse-broadening parameter (PBP) in lossy media are defined to analyze the propagation

and deformation of pulses in a dispersive lossy medium. Scenarios resembling typical GPR operation are simulated to demonstrate the efficacy of the proposed method. This article is organized as follows. A dispersive FDTD scheme with medium characterized by QCRF is presented in Section II, the implementation of a dispersive SIBC on one side of a dispersive lossy medium is presented in Section III, the PBP and group delay in a dispersive lossy medium are elaborated in Section IV, the simulation results are discussed in Section V, and some conclusions are drawn in Section VI.

II. DISPERSIVE FDTD SCHEME WITH A MEDIUM CHARACTERIZED BY QCRF

The relative permittivity of a dispersive lossy medium over a given frequency band can be approximated by a QCRF as

$$\epsilon_r(j\omega) = \frac{\alpha_0 + \alpha_1(j\omega) + \alpha_2(j\omega)^2}{1 + \beta_1(j\omega) + \beta_2(j\omega)^2} \quad (1)$$

where α_0 , α_1 , α_2 , β_1 , and β_2 are real coefficients, which are determined by applying a complex-curve fitting technique to measurement data as [24]

$$\begin{bmatrix} \alpha_0 \\ \alpha_1 \\ \alpha_2 \\ \beta_1 \\ \beta_2 \end{bmatrix} = \begin{bmatrix} \lambda_0 & 0 & -\lambda_2 & T_1 & S_2 \\ 0 & \lambda_2 & 0 & -S_2 & T_3 \\ \lambda_2 & 0 & -\lambda_4 & T_3 & S_4 \\ T_1 & -S_2 & -T_3 & U_2 & 0 \\ S_2 & T_3 & -S_4 & 0 & U_4 \end{bmatrix}^{-1} \begin{bmatrix} S_0 \\ T_1 \\ S_2 \\ 0 \\ U_2 \end{bmatrix}$$

where

$$\lambda_n = \sum_{k=0}^m \omega_k^n, \quad S_n = \sum_{k=0}^m \omega_k^n \epsilon'_{rk}$$

$$T_n = \sum_{k=0}^m -\omega_k^n \epsilon''_{rk}, \quad U_n = \sum_{k=0}^m \omega_k^n (\epsilon'^2_{rk} + \epsilon''^2_{rk})$$

$\epsilon_{rk} = \epsilon'_{rk} - j\epsilon''_{rk}$ is the relative permittivity at sampling frequency ω_k .

The electric flux density (\bar{D}) is related to the electric field (\bar{E}) by the constitutive relation as

$$\bar{D}(\omega) = \epsilon_0 \frac{\alpha_0 + \alpha_1(j\omega) + \alpha_2(j\omega)^2}{1 + \beta_1(j\omega) + \beta_2(j\omega)^2} \bar{E}(\omega)$$

which is transformed to the time domain as

$$\bar{D} + \beta_1 \frac{\partial \bar{D}}{\partial t} + \beta_2 \frac{\partial^2 \bar{D}}{\partial t^2} = \epsilon_0 \left(\alpha_0 \bar{E} + \alpha_1 \frac{\partial \bar{E}}{\partial t} + \alpha_2 \frac{\partial^2 \bar{E}}{\partial t^2} \right). \quad (2)$$

By applying a central difference scheme, (2) is discretized as

$$\begin{aligned} & \frac{\bar{D}^{n+1} + 2\bar{D}^n + \bar{D}^{n-1}}{4} + \frac{\beta_1}{2\Delta t} (\bar{D}^{n+1} - \bar{D}^{n-1}) \\ & + \frac{\beta_2}{(\Delta t)^2} (\bar{D}^{n+1} - 2\bar{D}^n + \bar{D}^{n-1}) \\ & = \epsilon_0 \left[\alpha_0 \frac{\bar{E}^{n+1} + 2\bar{E}^n + \bar{E}^{n-1}}{4} + \frac{\alpha_1}{2\Delta t} (\bar{E}_t^{n+1} - \bar{E}_t^{n-1}) \right. \\ & \left. + \frac{\alpha_2}{(\Delta t)^2} (\bar{E}^{n+1} - 2\bar{E}^n + \bar{E}^{n-1}) \right] \end{aligned} \quad (3)$$

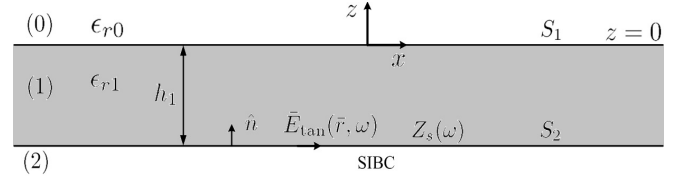


Fig. 1. Scattering from a two-layered medium, layer (0) is air, layer (1) is the vadose zone with thickness h_1 , layer (2) is an aquifer, and SIBC is implemented at an interface S_2 between layers (1) and (2).

where a double-averaging technique [12] is used to implement \bar{D} as $\bar{D} = (\bar{D}^{n+1} + 2\bar{D}^n + \bar{D}^{n-1})/4$, instead of $\bar{D} = \bar{D}^n$. Equation (3) is then rearranged as

$$\bar{E}^{n+1} = \gamma_1 \bar{E}^n + \gamma_2 \bar{E}^{n-1} + \gamma_3 \bar{D}^{n+1} + \gamma_4 \bar{D}^n + \gamma_5 \bar{D}^{n-1}$$

where

$$\begin{aligned} \gamma_1 &= -2 \frac{\zeta_0 - \zeta_2}{\zeta_0 + \zeta_1 + \zeta_2}, & \gamma_2 &= -\frac{\zeta_0 - \zeta_1 + \zeta_2}{\zeta_0 + \zeta_1 + \zeta_2} \\ \gamma_3 &= \frac{\zeta_0 + \zeta_1 + \zeta_2}{\zeta_0 + \zeta_1 + \zeta_2}, & \gamma_4 &= 2 \frac{\zeta_0 - \zeta_2}{\zeta_0 + \zeta_1 + \zeta_2} \\ \gamma_5 &= \frac{\zeta_0 - \zeta_1 + \zeta_2}{\zeta_0 + \zeta_1 + \zeta_2} \\ \zeta_0 &= \alpha_0 (\Delta t)^2, & \zeta_1 &= 2\alpha_1 \Delta t, & \zeta_2 &= 4\alpha_2 \\ \zeta_0 &= \frac{(\Delta t)^2}{\epsilon_0}, & \zeta_1 &= \frac{2\beta_1 \Delta t}{\epsilon_0}, & \zeta_2 &= \frac{4\beta_2}{\epsilon_0}. \end{aligned}$$

III. IMPLEMENTATION OF THE TIME-DOMAIN SIBC

Fig. 1 shows a two-layered medium, with a vadose zone between air and aquifer. A dispersive SIBC is implemented at the interface S_2 between layers (1) and (2). If a uniform plane wave (UPW) at frequency ω is incident upon S_1 , at an incident angle θ_0 , the SIBC at S_2 can be represented as [22]

$$\bar{E}_{\tan}(\bar{r}, \omega) = \frac{Z_s(j\omega)}{j\omega} \hat{n} \times j\omega \bar{H}(\bar{r}, \omega) \quad (4)$$

where $\bar{E}_{\tan}(\bar{r}, \omega) = \bar{E}(\bar{r}, \omega) - \hat{n} \hat{n} \cdot \bar{E}(\bar{r}, \omega)$, and

$$Z_s(j\omega) = \frac{\eta_0}{\sqrt{\epsilon_{r2}(j\omega)}}$$

is the surface impedance, which is valid under the condition that $|k_2| \gg k_{0x}$ ($|\epsilon_{r2}| \gg \sin^2 \theta_0$) [25], where η_0 is the intrinsic impedance in free space, and $\epsilon_{r2}(j\omega) = \epsilon'_{r2}(j\omega) - j\epsilon''_{r2}(j\omega)$ is the complex permittivity in layer (2).

Define normalized surface impedance as

$$Z'_s(j\omega) = \frac{Z_s(j\omega)}{j\omega} = \frac{\eta_0}{j\omega \sqrt{\epsilon_{r2}(j\omega)}} \quad (5)$$

which is curve-fit to another QCRF over a given frequency band as [24]

$$Z'_s(j\omega) = \frac{\alpha'_0 + \alpha'_1(j\omega)}{1 + \beta'_1(j\omega) + \beta'_2(j\omega)^2} \quad (6)$$

with

$$\begin{bmatrix} \alpha'_0 \\ \alpha'_1 \\ \beta'_1 \\ \beta'_2 \end{bmatrix} = \begin{bmatrix} \lambda'_0 & 0 & T'_1 & S'_2 \\ 0 & \lambda'_2 & -S'_2 & T'_3 \\ T'_1 & -S'_2 & U'_2 & 0 \\ S'_2 & T'_3 & 0 & U'_4 \end{bmatrix}^{-1} \begin{bmatrix} S'_0 \\ T'_1 \\ 0 \\ U'_2 \end{bmatrix}$$

where

$$\begin{aligned} \lambda'_n &= \sum_{k=0}^m \omega_k^n, & S'_n &= \sum_{k=0}^m \omega_k^n \text{Re}\{Z'_s\} \\ T'_n &= \sum_{k=0}^m \omega_k^n \text{Im}\{Z'_s\} \\ U'_n &= \sum_{k=0}^m \omega_k^n [(\text{Re}\{Z'_s\})^2 + (\text{Im}\{Z'_s\})^2]. \end{aligned}$$

By relabeling $j\omega$ as s , the normalized surface impedance in (6) is transformed to the Laplace domain as

$$Z'_s(s) = d \frac{s + \ell}{(s - a)^2 - b^2} \quad (7)$$

with $d = \alpha'_1/\beta'_2$, $\ell = \alpha'_0/\alpha'_1$, $a = -\beta'_1/(2\beta'_2)$ and $b = \sqrt{\beta_1'^2 - 4\beta_2'(2\beta_2')} > 0$. By applying an inverse Laplace transform to (7), we obtain a time-domain expression for implementing the normalized surface impedance as

$$\begin{aligned} Z'_s(t) &= d \left[e^{at} \cosh(bt) + \frac{a - \ell}{b} e^{at} \sinh(bt) \right] \\ &= d \left[\frac{b + a - \ell}{2b} e^{(a+b)t} + \frac{b - a + \ell}{2b} e^{(a-b)t} \right]. \end{aligned} \quad (8)$$

Next, (4) is transformed to the time domain as

$$\bar{E}_{\tan}(\bar{r}, t) = Z'_s(t) * \left[\hat{n} \times \frac{\partial \bar{H}(\bar{r}, t)}{\partial t} \right] \quad (9)$$

where $*$ is the convolution operator. By substituting (8) into (9), the time-domain implementation of SIBC is derived as

$$\begin{aligned} \bar{E}_{\tan}(\bar{r}, t) &= \int_0^t d \left[\frac{b + a - \ell}{2b} e^{(a+b)\tau} + \frac{b - a + \ell}{2b} e^{(a-b)\tau} \right] \hat{n} \times \frac{\partial \bar{H}}{\partial t'} \Big|_{t'=t-\tau} d\tau. \end{aligned} \quad (10)$$

The convolutional integral is computed as

$$\begin{aligned} \int_0^t g(\tau) h(t - \tau) d\tau &\simeq \int_0^{n\Delta t} g(\tau) h(n\Delta t - \tau) d\tau \\ &= \Delta t \sum_{m=0}^{n-1} \int_m^{m+1} g[u] h[n - u] du \end{aligned} \quad (11)$$

where $g[u] = g(u\Delta t)$ and $h[n - u] = h(n\Delta t - u\Delta t) \simeq h[n - m - 1](u - m) + h[n - m](1 - u + m)$. By using (11) and making an approximation

$$\left(\frac{\partial \bar{H}}{\partial t'} \right)^{n-u} \simeq \left(\frac{\partial \bar{H}}{\partial t'} \right)^{n-m-1} \simeq \frac{\bar{H}^{n-m-1/2} - \bar{H}^{n-m-3/2}}{\Delta t}.$$

Equation (10) is reduced to

$$\bar{E}_{\tan}^n = \sum_{m=0}^{n-1} \chi^m \hat{n} \times (\bar{H}^{n-m-1/2} - \bar{H}^{n-m-3/2})$$

where $\bar{E}_{\tan}^n = \bar{E}_{\tan}(n\Delta t)$, $\bar{H}^{n-m-1/2} = \bar{H}((n-m-1/2)\Delta t)$ and

$$\begin{aligned} \chi^m &= \int_m^{m+1} d \left[\frac{b + a - \ell}{2b} e^{(a+b)u\Delta t} + \frac{b - a + \ell}{2b} e^{(a-b)u\Delta t} \right] du \\ &= \frac{d(b + a - \ell)}{2b} \left[e^{(a+b)(m+1)\Delta t} - e^{(a+b)m\Delta t} \right] \\ &\quad + \frac{d(b - a + \ell)}{2b} \left[e^{(a-b)(m+1)\Delta t} - e^{(a-b)m\Delta t} \right]. \end{aligned}$$

IV. PULSE-BROADENING PARAMETER AND GROUP DELAY IN A DISPERSIVE LOSSY MEDIUM

PBP is defined to characterize the stretching (deformation) of a time-domain pulse as it propagates in a dispersive lossy medium. Consider a Gaussian-modulated time-harmonic pulse emitted at $z = 0$

$$E(0, t) = E_0 e^{-t^2/\tau_0^2} e^{j\omega_c t} = E_0 e^{-t^2/(a_1^2 \tau^2)} e^{j\omega_c t}$$

where ω_c is the carrier frequency, τ_0 is the time scale for the magnitude of pulse envelope to decrease by a factor of e , and $\tau = \tau_0/a_1$ (with $a_1 = \sqrt{2/\ln 2}$) is the half-power time scale for the magnitude to decrease by a factor of $\sqrt{2}$. A pulse propagating along the z -direction in a dispersive lossless medium can be represented as [26, p. 642]

$$E(z, t) = E_0 \frac{e^{j(\omega_c t + k_z^{(0)} z)}}{\sqrt{1 + j(S/\tau)}} e^{-(t-t_c)^2(1-jS/\tau)/[a_1^2(\tau^2 + S^2)]} \quad (12)$$

where $k_z^{(0)} = k_z(\omega_c)$, $t_c = z(dk_z/d\omega)|_{\omega_c}$ is the group delay at ω_c , and $S = (2/a_1^2 \tau) k_z^{(2)} z$ is the PBP, with $k_z^{(2)} = (d^2 k_z/d\omega^2)|_{\omega_c}$. Note that S is related to the PBP (S_0) defined in [26] by $S = S_0/a_1$.

The wavenumber in a lossy medium is complex, $k = k' - jk''$, which implies that t_c and S are also complex, namely $t_c = t'_c - jt''_c$ and $S = S' - jS''$. Thus, the magnitude of the last exponential term in (12) becomes

$$\begin{aligned} |e^{-(t-t_c)^2(1-jS/\tau)/[a_1^2(\tau^2 + S^2)]}| &= |e^{(R_n - jI_n)/(R_d - jI_d)}| \\ &= e^{(R_n R_d + I_n I_d)/(R_d^2 + I_d^2)} \end{aligned} \quad (13)$$

where

$$\begin{aligned} R_n &= [-(t - t'_c)^2 + t''_c{}^2] \left(1 - \frac{S''}{\tau} \right) - 2(t - t'_c) t''_c \frac{S'}{\tau} \\ I_n &= 2t''_c (t - t'_c) \left(1 - \frac{S''}{\tau} \right) - (t - t'_c)^2 \frac{S'}{\tau} + t''_c{}^2 \frac{S'}{\tau} \\ R_d &= a_1^2 (\tau^2 + S'^2 - S''^2), & I_d &= 2a_1^2 S' S''. \end{aligned}$$

The time elapse T it takes for the peak magnitude to decrease by a factor of $\sqrt{2}$ is determined from (13) as

$$T^2 = a_1^2 \frac{(\tau^2 + S'^2 - S''^2)^2 + 4S'^2 S''^2}{(1 - S''/\tau)(\tau^2 + S'^2 - S''^2) + 2S'^2 S''/\tau}$$

which reduces to

$$T^2 = a_1^2(\tau^2 + S'^2) \quad (14)$$

if the medium is lossless ($k'' = 0$, $S'' = 0$). Following the same functional form in (14), the PBP in a dispersive lossy medium is defined as:

$$S_\ell = \text{sgn}\{T/a_1 - \tau\} \sqrt{|T^2/a_1^2 - \tau^2|}$$

which means the pulse is stretched ($S_\ell > 0$) if $T/a_1 > \tau$ and is compressed ($S_\ell < 0$) if $T/a_1 < \tau$.

To calculate $S = (2/a_1^2 \tau) k_z^{(2)} z$, with $k_z = k$ for a pulse propagating in the z -direction, we substitute the QCRF model of $\epsilon_r(\omega)$ in (1) into $k = \omega \sqrt{\mu_0 \epsilon_0 \epsilon_r(\omega)}$ to derive

$$k_z^{(2)} = \frac{1}{c} \epsilon_r^{-1/2}(\omega) \frac{d\epsilon_r}{d\omega} - \frac{\omega}{4c} \epsilon_r^{-3/2}(\omega) \left(\frac{d\epsilon_r}{d\omega} \right)^2 + \frac{\omega}{2c} \epsilon_r^{-1/2}(\omega) \frac{d^2\epsilon_r}{d\omega^2}$$

where c is the speed of light in free space, $d\epsilon_r/d\omega = U/Q^2$ and $d^2\epsilon_r/d\omega^2 = -2(QV + WU)/Q^3$, with

$$\begin{aligned} Q &= 1 + \beta_1(j\omega) + \beta_2(j\omega)^2 \\ U &= j(\alpha_1 - \alpha_0\beta_1) - 2(\alpha_2 - \alpha_0\beta_2)\omega - j(\alpha_2\beta_1 - \alpha_1\beta_2)\omega^2 \\ V &= (\alpha_2 - \alpha_0\beta_2) + j(\alpha_2\beta_1 - \alpha_1\beta_2)\omega \\ W &= j\beta_1 - 2\beta_2\omega. \end{aligned}$$

The group velocity in a dispersive lossy medium is defined as $v_g = (dk'/d\omega)^{-1}$, where $k = \sqrt{\epsilon_r(\omega)}\omega/c = k' - jk''$ and

$$\frac{dk}{d\omega} = \frac{\sqrt{\epsilon_r(\omega)}}{c} + \frac{\omega}{2c\sqrt{\epsilon_r(\omega)}} \frac{d\epsilon_r(\omega)}{d\omega} \quad (15)$$

of which the real part is

$$\begin{aligned} \frac{dk'}{d\omega} &= \frac{\text{Re}\{\sqrt{\epsilon_r(\omega)}\}}{c} + \frac{\omega}{2c} \\ &\times \left(\text{Re} \left\{ \frac{1}{\sqrt{\epsilon_r(\omega)}} \right\} \frac{d\epsilon_r'(\omega)}{d\omega} + \text{Im} \left\{ \frac{1}{\sqrt{\epsilon_r(\omega)}} \right\} \frac{d\epsilon_r''(\omega)}{d\omega} \right) \\ &= \frac{\text{Re}\{\sqrt{\epsilon_r(\omega)}\}}{c} + \frac{\omega}{2c} \\ &\times \left(\frac{\text{Re}\{\sqrt{\epsilon_r(\omega)}\} d\epsilon_r'(\omega)}{|\epsilon_r| d\omega} - \frac{\text{Im}\{\sqrt{\epsilon_r(\omega)}\} d\epsilon_r''(\omega)}{|\epsilon_r| d\omega} \right). \end{aligned}$$

The group delay (t_g) for a pulse to propagate in the dispersive lossy medium over a distance z is $t_g = z/v_g$. If the medium is nondispersive ($d\epsilon_r/d\omega = 0$), the group velocity becomes the same as the phase velocity, namely $v_g = c/\text{Re}\{\sqrt{\epsilon_r}\} = v_p$ [27].

V. SIMULATIONS AND DISCUSSION

In this section, we first check the efficacy of replacing a half-space dispersive medium with a dispersive SIBC. Then, backscattered pulse from a dispersive aquifer below a dispersive soil layer is simulated. Finally, backscattered fields from an object immersed in a dispersive soil are demonstrated.

Fig. 2 shows a schematic to simulate GPR operation in detecting underground texture or immersed objects. A tapered plane wave (TPW) is emitted downward upon a virtual surface S_v , which has an area of $L_{vx} \times L_{vy}$ and is located

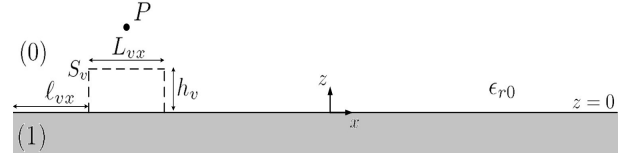


Fig. 2. Schematic to simulate GPR operation.

at h_v above the ground. The time-domain scattered fields at point P above S_v are recorded and interpreted as the echoed signals. We choose $(L_{vx}, L_{vy}, h_v) = (\lambda, \lambda, 0.1\lambda)$, where λ is the wavelength in free space at the carrier frequency f_c . To simulate typical GPR operation, the surface S_v is laterally shifted to a specific location, followed by the computation of scattered fields with the proposed FDTD scheme, then shifted to the next location, and so on. The cross section of the computational domain in the xy plane is chosen to be $L_x \times L_y = 8\lambda \times 8\lambda$. The electric field of the incident TPW takes the form of

$$\begin{aligned} \vec{E}_i(\vec{r}, t) &= \hat{p} E_0 G_{\text{tap}}(\vec{r}) \cos\{\omega_c[(t - t_0) - \hat{k}_i \cdot (\vec{r} - \vec{r}_0)/v_p]\} \\ &\times e^{-[(t-t_0) - \hat{k}_i \cdot (\vec{r} - \vec{r}_0)/v_p]^2/\tau_0^2} \quad (16) \end{aligned}$$

where \vec{r}_0 is at the center of S_v . The Gaussian tapering function $G_{\text{tap}}(\vec{r})$ is the product of two Gaussian functions in $\hat{\phi}$ and $\hat{\theta}$ directions, namely [11]

$$G_{\text{tap}}(\vec{r}) = e^{-d_{\hat{\theta}}^2(\vec{r}, \hat{k}_i)/(2r_a^2)} e^{-d_{\hat{\phi}}^2(\vec{r}, \hat{k}_i)/(2r_b^2)}.$$

The Fourier transform of (16) is

$$\begin{aligned} \vec{E}_i(\vec{r}, \omega) &= \hat{p} E'_0 G_{\text{tap}}(\vec{r}) e^{-j\omega[t_0 + \hat{k}_i \cdot (\vec{r} - \vec{r}_0)/v_p]} \\ &[e^{-\tau_0^2(\omega - \omega_c)^2/4} + e^{-\tau_0^2(\omega + \omega_c)^2/4}] \quad (17) \end{aligned}$$

where $E'_0 = E_0 \tau_0 \sqrt{\pi}/2$, \hat{p} is the polarization of the incident electric field, which is chosen to be \hat{y} in this article.

Fig. 3(a) shows the relative permittivity of a soil sample (Avra Valley, $m_v = 10.6\%$) at frequencies of 100–900 MHz. Fig. 3(b) shows the normalized surface impedance Z'_s by substituting the measured data in Fig. 3(a) into (5), followed by complex curve fitting.

Fig. 4 shows the backscattered field at P from a dispersive half-space medium characterized by the data in Fig. 3. The frequency spectrum of the incident TPW falls in 100–900 MHz, centered at $f_c = 500$ MHz. It is observed that the waveform of the backscattered field computed with the proposed dispersive SIBC is close to that with the dispersive FDTD scheme, especially at early times.

The dispersive FDTD scheme applies to a dispersive half-space medium and the dispersive SIBC scheme applies on the interface above a dispersive half-space medium. Both schemes are based on the same dispersive relation in (1). The dispersive FDTD scheme applies (1) in the lower half-space, with the discretization scheme in (3). The dispersive SIBC scheme applies (1) to the effective surface impedance in (5) to derive (6), which is then implemented in the time domain in (10). This may account for the deviation in their later-time responses, which still exists when finer FDTD grid size is adopted. In this article, the SIBC is claimed

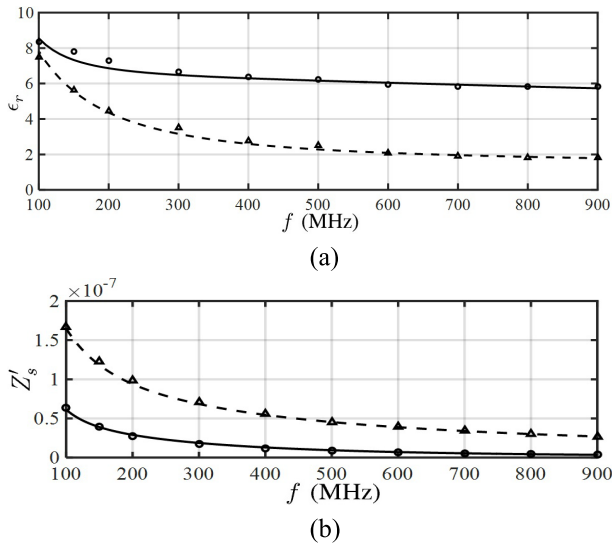


Fig. 3. (a) Relative permittivity of soil sample (Avra Valley), $m_v = 10.6\%$ [28]. \circ : measured ϵ_r' . —: curve fitting of ϵ_r' . Δ : measured ϵ_r'' . - - -: curve fitting of ϵ_r'' . (b) Normalized surface impedance Z'_s corresponding to the measured data in (a). \circ : $\text{Re}\{Z'_s\}$ of the measured ϵ_r . Δ : $-\text{Im}\{Z'_s\}$ of the measured ϵ_r . —: curve fitting of $\text{Re}\{Z'_s\}$. - - -: curve fitting of $-\text{Im}\{Z'_s\}$.

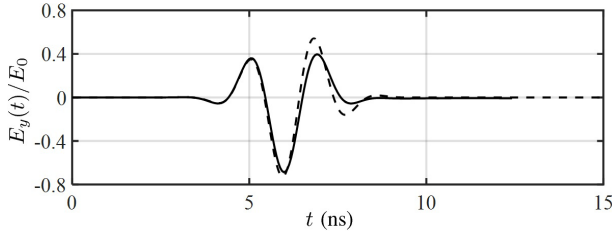


Fig. 4. Backscattered field at P from a dispersive half-space medium characterized by data in Fig. 3. —: dispersive SIBC. - - -: dispersive FDTD.

to save computational cost by replacing a half-space with an effective impedance boundary condition. The deviation in later-time responses is believed to be modeling error attributed to different approximations adopted in the dispersive FDTD scheme and the dispersive SIBC scheme.

In the dispersive FDTD scheme, (2) is implemented to all the Yee cells in the half-space medium. In the dispersive SIBC, (6) is implemented on the interface above the half-space medium. The functional forms of (2) and (6) are similar, implying similar amount of computational cost. Consider an interface composed of $N_x \times N_y$ pixels, and the half-space medium has the depth of N_z intervals. Then, (2) in the dispersive FDTD scheme is executed $O(N_x N_y N_z)$ times and (6) in the dispersive SIBC scheme is executed $O(N_x N_y)$ times. The CPU time and memory requirement of both schemes differ by an order of N_z .

One may wonder which scheme provides more accurate later-time response in Fig. 4. The deviation in later-time responses is believed to be model specific, which may be attributed to different approximations adopted in the dispersive FDTD scheme and the dispersive SIBC scheme, respectively. In other words, these two schemes are not exactly equivalent.

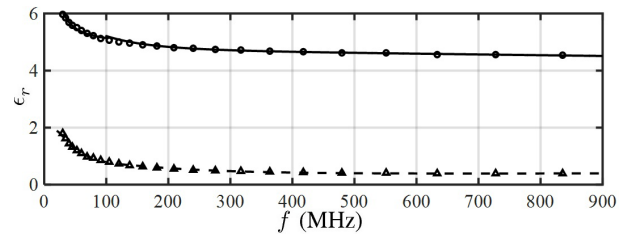


Fig. 5. Relative permittivity of soil sample (Puerto Rico clay loam), $m_v = 5\%$ [29]. \circ : measured ϵ_r' . —: curve fitting of ϵ_r' . Δ : measured ϵ_r'' . - - -: curve fitting of ϵ_r'' .

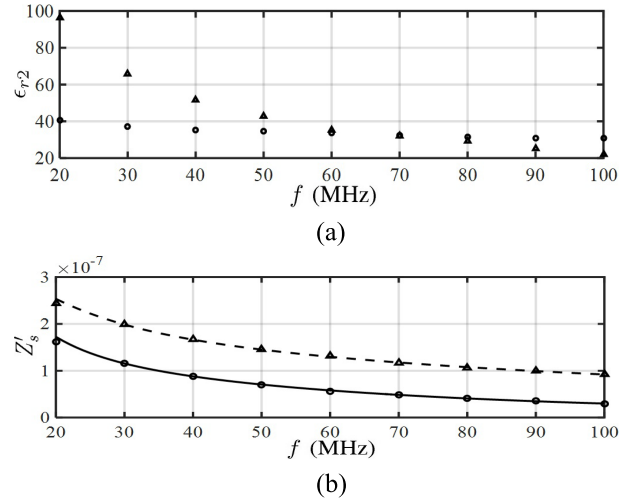


Fig. 6. (a) Relative permittivity of soil in Avra Valley, $m_v = 45.5\%$ [28]. \circ : measured ϵ_{r2}' . Δ : measured ϵ_{r2}'' . (b) Normalized surface impedance $Z'_s(j\omega)$ corresponding to the measured data in (a). \circ : $\text{Re}\{Z'_s\}$ of the measured ϵ_{r2} . Δ : $-\text{Im}\{Z'_s\}$ of the measured ϵ_{r2} . —: curve fitting of $\text{Re}\{Z'_s\}$. - - -: curve fitting of $-\text{Im}\{Z'_s\}$.

Either scheme is based on a QCRF approximation, and the two QCRF approximations are not directly related to each other. In addition, both schemes are used to compute the pulse response of GPR in a dispersive and highly conductive medium, which makes the comparison more complicated than in the case of nondispersive or low-loss media. One possible exploration is to consider higher order QCRFs in both schemes to conduct further comparison, starting from nondispersive or low-loss media. In summary, the dispersive SIBC scheme can significantly save the computational load, but the later-time response should be used with caution as far as the accuracy is of concern.

Fig. 5 shows the relative permittivity of another soil sample (Puerto Rico clay loam, $m_v = 5\%$) over the frequency band of 20–900 MHz, which is derived by curve-fitting the measured data at specific frequencies. The data will be used to characterize the (relatively dry) soil layer in the following simulations.

Next, the proposed dispersive SIBC is implemented at the interface between soil and aquifer. Fig. 6(a) shows the relative permittivity (over frequencies 20–100 MHz) of a (relatively wet) soil sample in the Avra Valley, which has moisture content of $m_v = 45.5\%$ [28] and is used to model the aquifer.

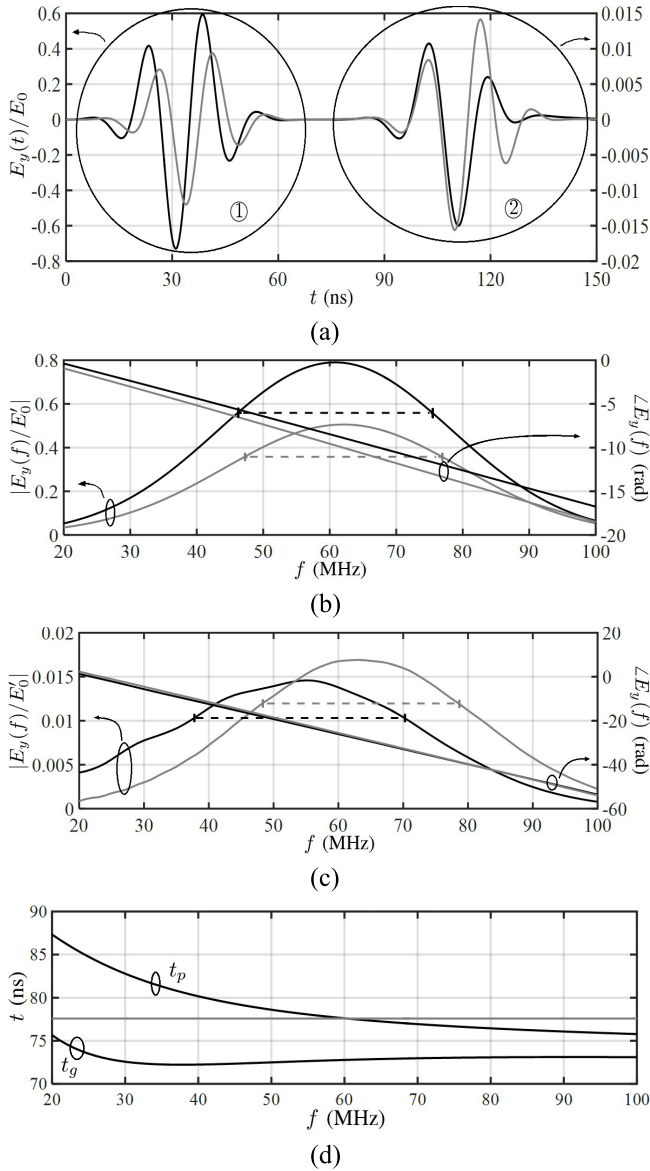


Fig. 7. Backscattered signals at P from an aquifer below a soil layer, $f_c = 60$ MHz. —: dispersive media [ϵ_{r1} in Fig. 5 and ϵ_{r2} in Fig. 6(a)]. Gray: nondispersive media ($\epsilon_{r1} = 5.36 - j1.11$ and $\epsilon_{r2} = 33.84 - j35.3$). — —: Half-power bandwidth. (a) Time-domain backscattered field. (b) Frequency-domain amplitude and phase of pulse ① (c) Amplitude and phase of pulse ② (d) Group delay t_g and phase delay t_p . $t_g = t_p = 77.58$ ns in nondispersive media.

Fig. 6(b) shows the normalized surface impedance on the top surface of an aquifer. The maximum deviation between $\text{Re}\{Z'_s\}$ derived from the measured ϵ_{r2} and its counterpart from curve-fitting is 6.2%, which appears at 20 MHz. The maximum deviation in $-\text{Im}\{Z'_s\}$ is 3.7%, which also appears at 20 MHz. The deviations in both $\text{Re}\{Z'_s\}$ and $-\text{Im}\{Z'_s\}$ are less than 0.5% at frequencies higher than 30 MHz. The coefficients in (6), associated with the curves in Fig. 6(b), are $\alpha'_0 = 7.3101 \times 10^{-7}$, $\alpha'_1 = 2.1244 \times 10^{-15}$, $\beta'_1 = 2.1429 \times 10^{-8}$, and $\beta'_2 = 4.5485 \times 10^{-17}$. The depth of water table is arbitrarily set to the global average value of $h_1 = 5$ m [30].

Fig. 7 shows the backscattered field from the aquifer below a soil layer. The power spectrum of the incident pulse falls

in 20–100 MHz, centered at $f_c = 60$ MHz. Fig. 7(a) shows that pulse ① is reflected from the air–soil interface, and pulse ② is reflected from the soil–aquifer interface (water table). The PBP of pulse ② is $S_\ell = -1.36$ ns, indicating compression as compared to its counterpart in nondispersive media.

Fig. 7(b) shows that the half-power bandwidth of pulse ① is about 28 MHz, no matter the media are dispersive or not. The difference in phase and amplitude between dispersive and nondispersive media is caused by the frequency dependence of backscattered fields. The linear relation between phase and frequency in both media is attributed to the time delay t_0 of the incident waveform in (17).

Fig. 7(c) shows the phase and magnitude of pulse ②. The bandwidth in the dispersive media is 32 MHz, wider than that in the nondispersive media of 29 MHz, which implies compression of time-domain pulse in the dispersive media. Fig. 7(d) shows the group delay and phase delay over the soil layer, with a round-trip distance of $2h_1 = 10$ m. It is observed that the phase delay of wave components at $f < f_c$ in the dispersive medium is longer than their counterparts in the nondispersive medium, up to 10 ns at $f = 20$ MHz. On the other hand, the phase delay of wave components at $f > f_c$ in the dispersive medium is shorter than their nondispersive counterparts, up to 1.8 ns at $f = 100$ MHz.

The field energy propagates at group velocity. It is observed that the wave components at $f < 30$ MHz move the slowest, those around $f = 38$ MHz move the fastest, and those at $f > 40$ MHz move at almost a constant speed. The differences in group delay among these three groups are less than 2.5 ns and have negligible effect on the waveform shown in Fig. 7(a). As a comparison, the group delay in the dispersive media is shorter than that in the nondispersive media by 2–5 ns. Also, notice that pulse ② in the nondispersive media maintains almost the same waveform as ①

Finally, we demonstrate a scenario resembling GPR operation to detect a rectilinear Plexiglas block with relative permittivity $\epsilon_{rb} = 2.6$ [15], horizontal dimensions (x - and y -directions) of $a = b = 60$ cm, and vertical dimension (z -direction) of $c = 9.6$ cm, immersed at a depth of $h_b = 60$ cm. Fig. 8(a) shows the backscattered field from the immersed block in dispersive and nondispersive soils. Pulse ① is reflected from the air–soil interface and pulse ② is from the Plexiglas block. Pulse ② in the dispersive soil is stretched by $S_\ell = 0.12$ ns, as compared to its counterpart in the nondispersive soil. The amplitude of pulse ② in the nondispersive medium is larger than in the dispersive medium. As shown in Fig. 5, the imaginary part of the soil permittivity in the dispersive soil is about $\epsilon''_{r1} = 0.4$ at $f > f_c$ and gradually increases to $\epsilon''_{r1} = 0.8$ at $f < f_c$, while that of the nondispersive soil is about $\epsilon''_{r1} = 0.4$ at all frequencies. More energy is lost in the dispersive soil than in the nondispersive one, leading to smaller amplitude in the former.

Fig. 8(b) shows that the half-power bandwidths of pulse ① in dispersive and nondispersive media are 270 and 280 MHz, respectively. The difference in amplitude and phase between the dispersive soil and the nondispersive soil is attributed to the frequency dependence of backscattered fields. Fig. 8(c) shows that the half-power bandwidth of pulse ② in the dispersive

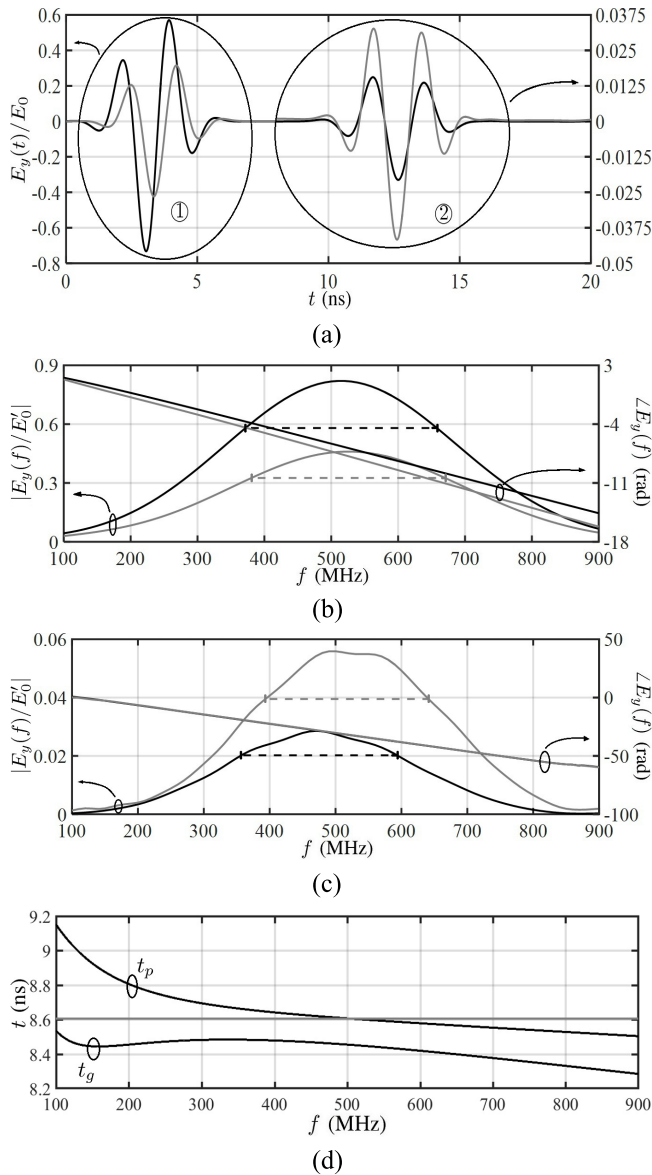


Fig. 8. Backscattered field at P right above the Plexiglas block ($\epsilon_{rb} = 2.6$) immersed 60 cm below ground surface, $f_c = 500$ MHz. —: dispersive soil. Gray: nondispersive soil with $\epsilon_{r1} = 4.62 - j0.4$. - - - indicates half-power bandwidth. (a) Time-domain backscattered field. (b) Amplitude and phase of pulse ① (c) Amplitude and phase of pulse ② (d) Group delay t_g and phase delay t_p , $t_g = t_p = 8.61$ ns in nondispersive media.

soil is 230 MHz, which is narrower than 240 MHz in the nondispersive soil, implying that the time-domain waveform in the former is wider than that in the latter.

Fig. 8(d) shows the group delay and phase delay in both dispersive and nondispersive soils over a round-trip distance of $2h_b = 120$ cm. The phase delay indicates that the wave components at $f < f_c = 500$ MHz move slower than that at f_c , up to 0.55 ns at $f = 100$ MHz. On the other hand, the wave components at $f > f_c$ move faster than that at f_c , up to 0.1 ns at $f = 900$ MHz.

The group delay in the dispersive soil indicates that the wave components at high frequencies move faster than those at low frequencies by 0.2 ns. In addition, the wave components in

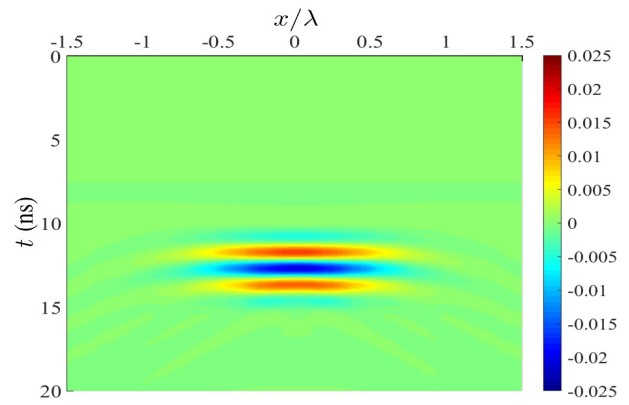


Fig. 9. Distribution of backscattered field (at $y = 0$) from an immersed block.

the dispersive soil arrive earlier than those in the nondispersive soil by 0.06–0.3 ns. The separation of high-frequency and low-frequency components is barely observable in Fig. 8(a) since the difference between their group delays is very small.

Fig. 8(a) shows that pulse ② in the nondispersive soil has different shape from pulse ① since the former is a superposition of reflected pulses from the top surface and the bottom surface of the immersed block. The traverse time from the top surface of the block to the air–soil interface is 4.3 ns and the traverse time for the pulse to bounce back and forth within the block is $2c/v_b = 1.03$ ns, where v_b is the speed of light in the block. The reflected pulse from the bottom surface of the block is superposed upon that from the top surface to form pulse ②

Fig. 9 shows the distribution of backscattered field (at $y = 0$) from an immersed block, which indicates the block is immersed in the range of $-0.5\lambda \leq x \leq 0.5\lambda$. The backscattered field from the air–soil interface is removed for the convenience of observation.

VI. CONCLUSION

A dispersive SIBC, represented in a QCRF form, is proposed to model a dispersive lossy medium with high permittivity and high conductivity. A dispersive FDTD scheme is implemented in conjunction with the dispersive SIBC to simulate the backscattered field distribution in the presence of water table or immersed object. A PBP for a dispersive lossy medium is proposed to characterize the stretch or compression of a time-domain pulse propagating in such medium. Measurement data from moistured soils are used to model an aquifer below a relatively dry soil layer. The proposed method has been used to analyze the effects of a dispersive lossy medium on pulse propagation in GPR operation to detect water table or immersed objects.

REFERENCES

- [1] M. Kovacevic, K. Gavin, I. S. Oslakovic, and M. Bacic, “A new methodology for assessment of railway infrastructure condition,” *Transp. Res. Procedia*, vol. 14, pp. 1930–1939, Jan. 2016.
- [2] O. Eisen, U. Nixdorf, L. Keck, and D. Wagenbach, “Alpine ice cores and ground penetrating radar: Combined investigations for glaciological and climatic interpretations of a cold Alpine ice body,” *Tellus B, Chem. Phys. Meteorol.*, vol. 55, no. 5, pp. 1007–1017, Dec. 2011.

- [3] J. J. Daniels, R. Roberts, and M. Vendl, "Ground penetrating radar for the detection of liquid contaminants," *J. Appl. Geophys.*, vol. 33, pp. 195–207, Jan. 1995.
- [4] Y. Nakashima, H. Zhou, and M. Sato, "Estimation of groundwater level by GPR in an area with multiple ambiguous reflections," *J. Appl. Geophys.*, vol. 47, nos. 3–4, pp. 241–249, Jul. 2001.
- [5] I. Giannakis, A. Giannopoulos, and C. Warren, "A realistic FDTD numerical modeling framework of ground penetrating radar for landmine detection," *IEEE J. Sel. Topics Appl. Earth Observ. Remote Sens.*, vol. 9, no. 1, pp. 37–51, Jan. 2016.
- [6] D. Uduwawala, M. Norgren, and P. Fuks, "A complete FDTD simulation of a real GPR antenna system operating above lossy and dispersive grounds," *Prog. Electromag. Res.*, vol. 50, pp. 209–229, 2005.
- [7] C. Warren, A. Giannopoulos, and I. Giannakis, "GprMax: Open source software to simulate electromagnetic wave propagation for ground penetrating radar," *Comput. Phys. Commun.*, vol. 209, pp. 163–170, Dec. 2016.
- [8] K. Yee, "Numerical solution of initial boundary value problems involving Maxwell's equations in isotropic media," *IEEE Trans. Antennas Propag.*, vol. AP-14, no. 3, pp. 302–307, May 1966.
- [9] A. Taflov and S. Hagness, *Computational Electrodynamics: The Finite-Difference Time-Domain Method*, 3rd ed. Norwood, MA, USA: Artech House, 2005.
- [10] A. K. Saxena and K. V. Srivastava, "Three-dimensional unconditionally stable LOD-FDTD methods with low numerical dispersion in the desired directions," *IEEE Trans. Antennas Propag.*, vol. 64, no. 7, pp. 3055–3067, Jul. 2016.
- [11] Z.-H. Lai, J.-F. Kiang, and R. Mittra, "A domain decomposition finite difference time domain (FDTD) method for scattering problem from very large rough surfaces," *IEEE Trans. Antennas Propag.*, vol. 63, no. 10, pp. 4468–4476, Oct. 2015.
- [12] S.-M. Park, E.-K. Kim, Y. B. Park, S. Ju, and K.-Y. Jung, "Parallel dispersive FDTD method based on the quadratic complex rational function," *IEEE Antennas Wireless Propag. Lett.*, vol. 15, pp. 425–428, 2015.
- [13] Q. H. Liu and G.-X. Fan, "Simulations of GPR in dispersive media using a frequency-dependent PSTD algorithm," *IEEE Trans. Geosci. Remote Sens.*, vol. 37, no. 5, pp. 2317–2324, Sep. 1999.
- [14] U. Oguz and L. Gurel, "Frequency responses of ground-penetrating radars operating over highly lossy grounds," *IEEE Trans. Geosci. Remote Sens.*, vol. 40, no. 6, pp. 1385–1394, Jun. 2002.
- [15] G. E. Atteia and K. F. A. Hussein, "Realistic model of dispersive soils using PLRC with applications to GPR systems," *Prog. Electromag. Res. B*, vol. 26, pp. 335–359, 2010.
- [16] S.-G. Ha, J. Cho, J. Choi, H. Kim, and K.-Y. Jung, "FDTD dispersive modeling of human tissues based on quadratic complex rational function," *IEEE Trans. Antennas Propag.*, vol. 61, no. 2, pp. 996–999, Feb. 2013.
- [17] H. Chung, J. Cho, S.-G. Ha, S. Ju, and K.-Y. Jung, "Accurate FDTD dispersive modeling for concrete materials," *ETRI J.*, vol. 35, no. 5, pp. 915–918, Oct. 2013.
- [18] H. Chung, K.-Y. Jung, X. T. Tee, and P. Bermel, "Time domain simulation of tandem silicon solar cells with optimal textured light trapping enabled by the quadratic complex rational function," *Opt. Express*, vol. 22, no. S3, pp. A818–A832, May 2014.
- [19] K.-Y. Jung, "On the numerical accuracy of finite-difference time-domain dispersive modeling based on a complex quadratic rational function," *Electromagnetics*, vol. 34, no. 5, pp. 380–391, Jul. 2014.
- [20] M. Leontovich, "Approximate boundary conditions for the electromagnetic field on the surface of a good conductor," *Invest. Radiowave Propag.*, vol. 2, pp. 5–12, 1948.
- [21] T. B. A. Senior, "Impedance boundary conditions for imperfectly conducting surfaces," *Appl. Sci. Res.*, vol. 8, no. 1, pp. 418–436, Dec. 1960.
- [22] J. Beggs, R. Luebbers, K. Yee, and K. Kunz, "Finite-difference time-domain implementation of surface impedance boundary conditions," *IEEE Trans. Antennas Propag.*, vol. 40, no. 1, pp. 49–56, Jan. 1992.
- [23] C. Penney, R. Luebbers, and J. Schuster, "Scattering from coated targets using a frequency-dependent, surface impedance boundary condition in FDTD," *IEEE Trans. Antennas Propag.*, vol. 44, no. 4, pp. 434–443, Apr. 1996.
- [24] E. C. Levy, "Complex-curve fitting," *IRE Trans. Automat. Control*, vol. AC-4, no. 1, pp. 37–43, May 1959.
- [25] J. Maloney and G. Smith, "The use of surface impedance concepts in the finite-difference time-domain method," *IEEE Trans. Antennas Propag.*, vol. 40, no. 1, pp. 38–48, Jan. 1992.
- [26] N. N. Rao, *Elements of Engineering Electromagnetics*. London, U.K.: Pearson, 2004.
- [27] Z.-H. Lai and J.-F. Kiang, "Brightness temperatures from very lossy medium with near-field bistatic transmission coefficients," *IEEE Trans. Geosci. Remote Sens.*, vol. 57, no. 7, pp. 4407–4416, Jul. 2019.
- [28] B. K. Sternberg and T. M. Levitskaya, "Electrical parameters of soils in the frequency range from 1 kHz to 1 GHz, using lumped-circuit methods," *Radio Sci.*, vol. 36, no. 4, pp. 709–719, Jul. 2001.
- [29] J. Hipp, "Soil electromagnetic parameters as functions of frequency, soil density, and soil moisture," *Proc. IEEE*, vol. 62, no. 1, pp. 98–103, Jan. 1974.
- [30] Y. Fan, H. Li, and G. Miguez-Macho, "Global patterns of groundwater table depth," *Science*, vol. 339, no. 6122, pp. 940–943, Feb. 2013.



Zhi-Hong Lai was born in Kaohsiung, Taiwan. He received the B.S. degree from the Department of Electrical Engineering, National Taiwan University, Taipei, Taiwan, in 2009 and the Ph.D. degree from the Graduate Institute of Communication Engineering, National Taiwan University in 2018.

Since 2019, he has been with MediaTek, Hsinchu, Taiwan. His research interests include finite-difference time-domain (FDTD) technique, wave scattering, propagation, and remote sensing.



Jean-Fu Kiang was born in Taipei, Taiwan, in 1957. He received the B.S.E.E. degree from National Taiwan University, Taipei, Taiwan, in 1979 and the Ph.D. degree in electrical engineering from the Massachusetts Institute of Technology, Cambridge, MA, USA, in 1989.

Since 1999, he has been a Professor with the Department of Electrical Engineering and the Graduate Institute of Communication Engineering, National Taiwan University. His research interests focus on electromagnetic applications and simulations, including transmission lines, antennas, phased arrays, propagation, scattering, radar signal processing, and remote sensing. Some of his works can be viewed in his website: http://cc.ee.ntu.edu.tw/~jfkang/selected_publications.html.